Resolution of distinct rotational substeps by submillisecond kinetic analysis of F_1-ATPase

Ryohei Yasuda*†‖, Hiroyuki Noji*, Masasuke Yoshida‡*, Kazuhiko Kinosita Jr†* & Hiroyasu Itoh§*

** CREST 'Genetic Programming' Team 13, Teikyo University Biotechnology Center 3F, Nogawa 907, Miyamae-Ku, Kawasaki 216-0001, Japan*
† Department of Physics, Faculty of Science and Technology, Keio University, Yokohama 223-8522, Japan
‡ Chemical Resources Laboratory, Tokyo Institute of Technology, Yokohama 226-8503, Japan
§ Tsukuba Research Laboratory, Hamamatsu Photonics KK, Tokodai, Tsukuba 300-2635, Japan

The enzyme F_1-ATPase has been shown to be a rotary motor in which the central γ-subunit rotates inside the cylinder made of $\alpha_3\beta_3$ subunits. At low ATP concentrations, the motor rotates in discrete 120° steps, consistent with sequential ATP hydrolysis on the three β-subunits. The mechanism of stepping is unknown. Here we show by high-speed imaging that the 120° step consists of roughly 90° and 30° substeps, each taking only a fraction of a millisecond. ATP binding drives the 90° substep, and the 30° substep is probably driven by release of a hydrolysis product. The two substeps are separated by two reactions of about 1 ms, which together occupy most of the ATP hydrolysis cycle. This scheme probably applies to rotation at full speed (~130 revolutions per second at saturating ATP) down to occasional stepping at nanomolar ATP concentrations, and supports the binding-change model for ATP synthesis by reverse rotation of F_1-ATPase.

The ATP synthase is an enzyme ubiquitous in bacteria, plants and animals, which synthesizes ATP from ADP and inorganic phosphate using proton flow through a membrane[1–3]. F_1, a water-soluble portion of the ATP synthase, is the site of ATP synthesis, whereas protons flow through the membrane-embedded F_o portion. At least *in vitro*, F_1 can hydrolyse ATP to pump protons through the F_o portion in the reverse direction. Isolated F_1 only hydrolyses ATP, and is called F_1-ATPase. Its subunit composition is $\alpha_3\beta_3\gamma\delta\epsilon$.

The prevailing view is that ATP hydrolysis/synthesis in F_1 is coupled to proton flow in F_o through the rotation of a common shaft, of which the γ-subunit of F_1 is a part. This rotational coupling mechanism was initially proposed by Boyer[1–3], and by others[4–6]. Later, a crystal structure of F_1 showed that a rod-shaped γ-subunit is surrounded by a cylinder made of three α- and three β-subunits, arranged alternately[7] (Fig. 1a). An analogue of ATP, ADP and none were bound to the three β-subunits, indicating that sequential ATP hydrolysis on the three β-subunits would indeed induce rotation of the central, asymmetrical γ-subunit. Rotation of the γ-subunit in an isolated F_1 during ATP hydrolysis has been demonstrated experimentally by various methods[8–10].

We have visualized the rotation of the γ-subunit under an optical microscope by fixing F_1 on a surface and attaching an actin filament to the γ-subunit as a marker of its orientation[10]. At nanomolar ATP, the actin filament rotated in discrete 120° steps[11], consistent with the pseudo-three-fold symmetrical structure[7] of F_1. The rotation rate was close to one-third of the rate of ATP hydrolysis in solution, suggesting that one ATP molecule is consumed per 120° step[11]. At high ATP concentrations, however, the actin rotation was smooth rather than stepwise, and the rotation was much slower than ATP hydrolysis. Viscous friction imposed on the actin filament prevented fast rotation of F_1 and obscured the stepping behaviour. Here we have used a smaller marker, a colloidal gold bead of 40-nm diameter, for which the viscous friction is 10^{-3} to 10^{-4} times that for actin (Fig. 1b). In the resultant high-speed rotation, we were able to resolve substeps. In this study we investigate the magnitudes, speeds, and timings of the substeps, and we also look at: (1) the motor speeds at no load; (2) whether the motor uses different rotary mechanisms at low and high speeds; (3) which parts of hydrolysis reactions drive the substeps; and (4) what structural changes may underlie the substeps.

Full-speed rotation with 40-nm beads

Bead rotation was imaged by laser dark-field microscopy[12] (Fig. 1c),

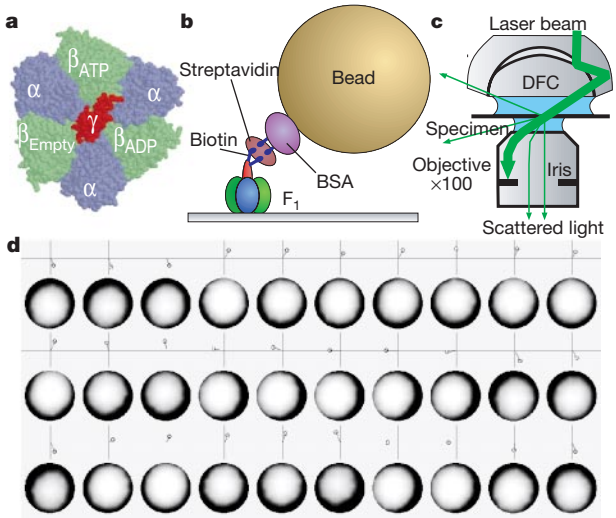

Figure 1 Observation of F_1 rotation. **a**, Atomic structure[7] of F_1-ATPase viewed from the F_o side (top in **b**). **b**, Side view of the observation system. The 40-nm bead gave a large enough optical signal that warranted a submillisecond resolution; but the bead was small enough not to impede the rotation. **c**, Laser dark-field microscopy for observation of gold beads. Only light scattered by the beads exited the objective and was detected. DFC, dark-field condenser. **d**, Sequential images of a rotating bead at 2 mM ATP. Images are trimmed in circles (diameter 370 nm) to aid identification of the bead position; centroid positions are shown above the images at ×3 magnification. The interval between images is 0.5 ms.

‖Present address: Cold Spring Harbor Laboratory, 1 Bungtown Road, Cold Spring Harbor, New York 11724, USA.

and recorded on a fast-framing charge-coupled-device (CCD) camera at speeds up to 8,000 frames per s. The 40-nm bead appeared as a spot of diffraction-limited size (~300 nm; Fig. 1d). When a bead is attached obliquely (Fig. 1b), rotation of the γ-subunit will result in a circular movement of the bead image. Some beads showed rotation (Fig. 1d; movies in Supplementary Information), and motions of these beads were analysed by calculating the centroid of the bead image[13]. The rotation diameter of bead centroid ranged between 25–55 nm. Diameters up to ~60 nm are possible for the height of F_1 of ~10 nm and the linker lengths of ~5 nm for streptavidin[14] and ~10 nm for BSA[15] (Fig. 1b). Rotation was stepwise at all ATP concentrations examined (see below).

To see whether the friction on the 40-nm bead impeded F_1 rotation, we varied the frictional load by attaching single or duplex polystyrene beads (108, 196 or 291 nm) to the γ-subunit. At both 2 mM and 2 μM ATP (Fig. 2; red and blue circles, respectively), time-averaged rotation rates showed saturation behaviour at small friction. Maximal rotation rate depended on ATP concentration [ATP], but increasing [ATP] beyond 2 mM did not accelerate rotation (see below). Thus, at 2 mM ATP, the 40-nm bead rotated at the full speed of the F_1 motor, which was 134 revolutions per second (r.p.s.) at 23 °C; the bead was not an impeding load for F_1. At saturating speeds, all beads rotated stepwise. On the load-dependent portions in Fig. 2, however, bead rotation was smooth, as was rotation of actin at these ATP concentrations[11]. The load dependence of actin rotation[11] (Fig. 2; triangles) is consistent with the bead assay.

One rotary mechanism at all speeds

The time-averaged rate of rotation showed simple Michaelis–Menten dependence on [ATP] (Fig. 3; the maximal rate at infinite [ATP], V_{max} = 129 r.p.s.; Michaelis constant, K_m = 15 μM), suggesting that one mechanism accounts for rotation in the nM–mM range. This idea is corroborated by observations[11,16,17] that the torque and its angle dependence, as well as mechanical work done in a 120° step, are independent of [ATP] over the nM–mM range. Also, the apparent rate of ATP binding, k_{on}^{ATP}, given by $3V_{max}/K_m$ of $(2.6 \pm 0.5) \times 10^7\ M^{-1}\ s^{-1}$ agrees with previous estimates based on the analysis of step intervals at nanomolar ATP[11,18].

As seen in Fig. 3, the rotation rate was close to one-third of the rate of ATP hydrolysis for bead-free F_1 in solution, supporting the contention that one ATP molecule is consumed per 120° rotation[11,16–18]. The hydrolysis rate, however, was lower, particularly around 50 μM. A probable cause is MgADP inhibition: F_1 is stochastically inactivated during ATP hydrolysis, when it binds MgADP tightly[17,19,20]. Although we started with nucleotide-free F_1, some inactivation may have proceeded during the mixing time of ~2 s. Indeed, the rate of inactivation increases with [ATP] and reaches ~0.3 s^{-1} at > 10 μM ATP[20], the position of the concavity in Fig. 3. Higher activity at still higher [ATP] is accounted for by binding of ATP to non-catalytic α-subunits, which tends to restore the hydrolysis activity[19]. Lauryldodecylamine oxide (LDAO), a suppressor of the MgADP inhibition[19], produced hydrolysis kinetics parallel to the rotation kinetics, although $V_{max}/3$ (82 s^{-1}) was only ~60% of V_{max} for rotation (Fig. 3).

The 120° step consists of 90° and 30° substeps

At 8,000 frames per s, steps were clearly resolved in the rotation of 40-nm beads, even at saturating ATP. At 2 mM ATP, only 120° steps were seen (Fig. 4a, b), whereas at 20 μM or 2 μM ATP, the 120° step was further split into roughly 90° and 30° substeps (Fig. 4c–f, where each panel shows a continuous record). We call the interval between a 30° substep and a 90° substep a '0° dwell' and the interval between 90° and 30° substeps a '90° dwell'. In Fig. 4c–f, 0° dwells fall on black horizontal lines that are separated from each other by 120°, and 90° dwells fall on grey lines that are 30° below the black lines. The 90° dwells were about a few ms in duration, on average, both at 2 and 20 μM ATP, whereas 0° dwells became longer at 2 μM. The implication is that F_1 waits for the arrival of ATP during the 0° dwell, which is terminated by a 90° substep induced by ATP binding. The subsequent 90° dwell is for a process or processes independent of [ATP]. This scheme predicts that, at [ATP] ~ K_m = 15 μM, 0° and 90° dwells have approximately equal lengths, as was observed

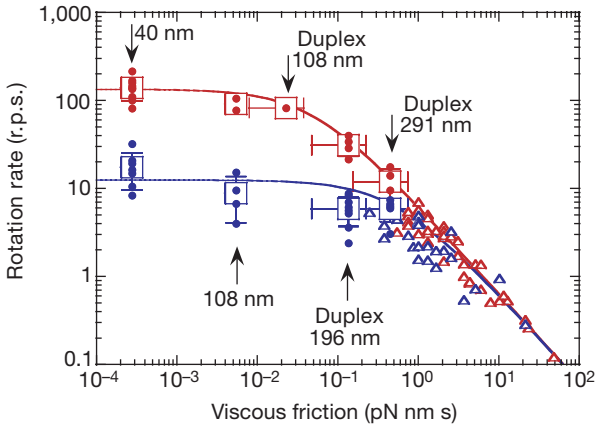

Figure 2 Relationship between rate of bead rotation and viscous friction on the bead. Circles, the average rate for a bead calculated over at least 20 consecutive revolutions; squares, the average over different beads (vertical error bars indicate s.d.). ATP at 2 mM and 2 μM is indicated by red and blue colours, respectively. The abscissa is the rotational frictional drag coefficient ξ calculated as in Methods. Possible range of ξ for each bead is shown by the size of the squares or associated horizontal error bars. For comparison, rotation rates for an actin filament attached to the γ-subunit[11] are also plotted (triangles). Lines show fits with the rate expected for a motor producing a constant torque[11]: $(1/V_{noload} + 2\pi\xi/N)^{-1}$ where N = 40 pN nm (assumed torque) and V_{noload} = 12.5 ± 1.0 r.p.s. for 2 μM ATP and 134 ± 3 r.p.s. for 2 mM ATP (s.e.m.).

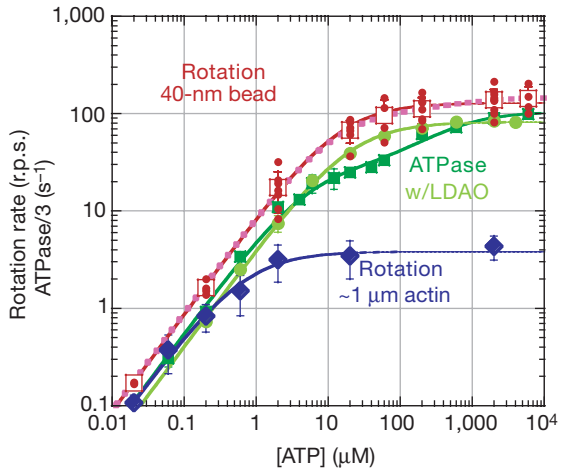

Figure 3 Comparison of rotation and hydrolysis rates. Red circles, time-averaged rotation rate for individual 40-nm beads. Red squares, rotation rate averaged over different beads. Dark green squares, one-third of the initial rate of ATP hydrolysis. Light green circles, one-third of the rate of ATP hydrolysis in the presence of LDAO. Blue diamonds, rotation rate for an actin filament attached to the γ-subunit[11]. Standard deviations greater than the symbol size are shown in bars ($n \geq 2$). Curves show fits with Michaelis–Menten kinetics, $V = V_{max}[ATP]/(K_m + [ATP])$, where V_{max} and K_m are 129 ± 9 r.p.s. and 15 ± 2 μM for bead rotation (red), 4.0 ± 0.3 r.p.s. and 0.7 ± 0.1 μM for actin rotation (blue), and 247 ± 9 s^{-1} and 19 ± 1 μM for hydrolysis in the presence of LDAO (light green). Fits with two K_m values, $V = (V_{max1}K_{m2}[ATP] + V_{max2}[ATP]^2)/([ATP]^2 + K_{m2}[ATP] + K_{m1}K_{m2})$, are also shown, where V_{max1} = 85 ± 9 s^{-1}, K_{m1} = 5.2 ± 0.7 μM, V_{max2} = 306 ± 22 s^{-1}, and K_{m2} = 393 ± 147 μM for hydrolysis without LDAO (dark green), and V_{max1} = 109 ± 30 r.p.s., K_{m1} = 12 ± 4 μM, V_{max2} = 149 ± 32 r.p.s., and K_{m2} = 682 ± 2768 μM for bead rotation (dashed pink). The latter does not show improvement over the simple fit in red. Values are means ± s.e.m.

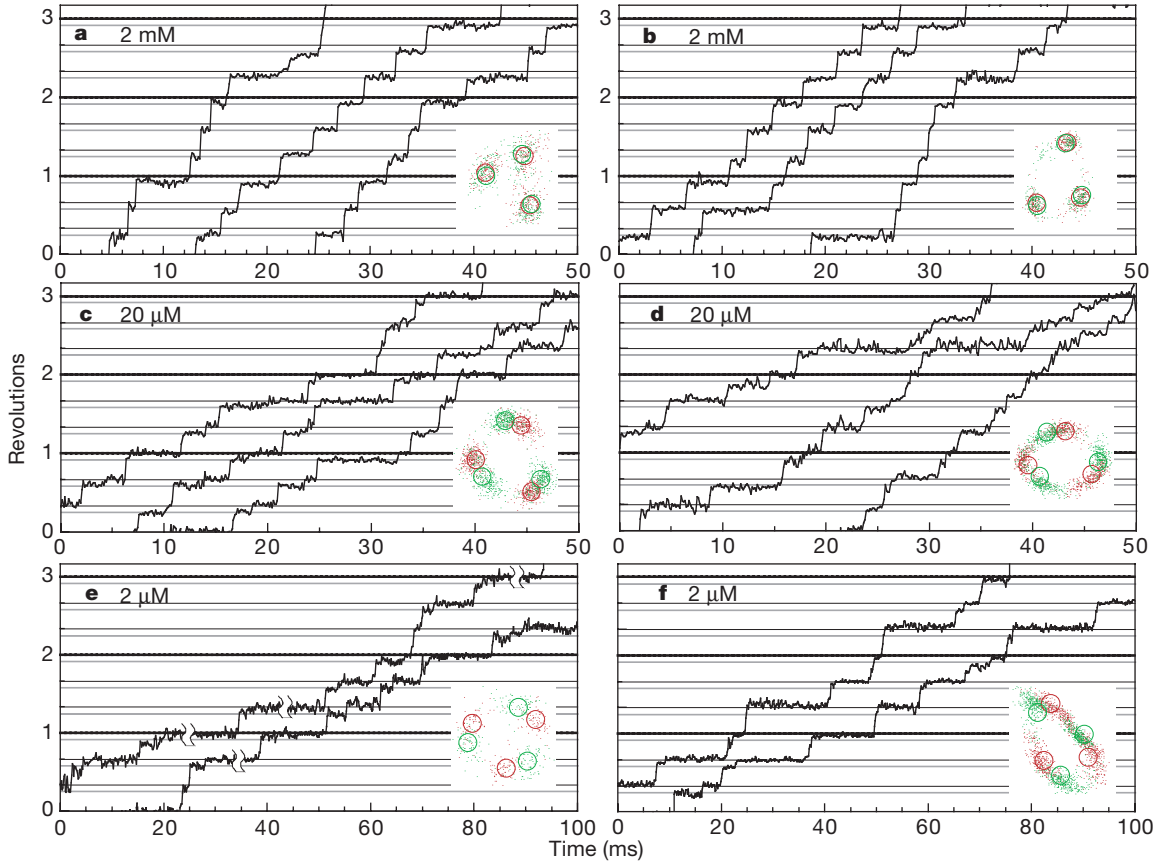

Figure 4 Unfiltered time courses of stepping rotation of 40-nm beads at varying [ATP]. **a**, **b**, 2 mM; **c**, **d**, 20 μM; **e**, **f**, 2 μM [ATP]. All curves in a panel are continuous; later curves are shifted, to save space. Grey horizontal lines are placed 30° below black lines. In **e**, some of the long dwells are cut short. Insets, positions of a bead within 0.25–0.5 ms before (red) and after (green) the main (90° or 120°) steps; runs lasting 0.5 s (2 mM) or 2 s (2 μM and 20 μM) were analysed. Circles indicate projection of ~0° and ~90° dwell points on an obliquely situated circular trajectory that best fit the data. Angles in the time courses and in Fig. 5 are those on the oblique circle.

at 20 μM ATP. At 2 mM ATP, the expected rate of ATP binding is $(2.6\times10^{7}\ M^{-1}s^{-1}\times2\ mM)\approx5\times10^{4}\ s^{-1}$. Then, 0° dwells will be ~0.02 ms and will not be detected at the current resolution. The absence of substeps in Fig. 4a, b is thus explained. We place dwells in Fig. 4a, b on grey lines, because they must be 90° dwells according to this explanation (see also Fig. 7).

The 30° substeps were not always clear, but we could easily locate, in rotation records, steps that spanned most of a 120° interval (~90° or ~120° step). Positions of the bead centroid in 0.25–0.5-ms intervals before (red) and after (green) these main steps are shown in the insets of Fig. 4. At 2 μM and 20 μM ATP, red and green spots are separated by ~30°, showing the presence of substeps, whereas spots overlap with each other at 2 mM ATP. The traces are distorted, presumably because of oblique rotation on an obliquely situated F_1. Circles on each trace are the projection of three equally spaced pairs of dwell positions on a circular trajectory oblique to the surface. A search for the best fit with the observed traces show the separation between red and green circles to be 29° ± 7° (mean ± s.d.) for 13 runs at 2, 6 and 20 μM ATP; and 4° ± 3° for 7 runs at 2 and 6 mM.

Figure 5 shows histograms of angular positions. Separations of peaks at 20 μM ATP (crosses) averaged 35° ± 13° (mean ± s.d. for 15 peak pairs). Substeps are less obvious at 2 μM, but histograms for the 2-ms intervals before and after the main steps (green) show similar peak separations. Taking these and other experimental uncertainties into account, we estimate the substep sizes to be within 90° ± 10° and 30° ± 10°.

Steps are fast

Consecutive steps in a rotation record at 2 mM ATP are super-

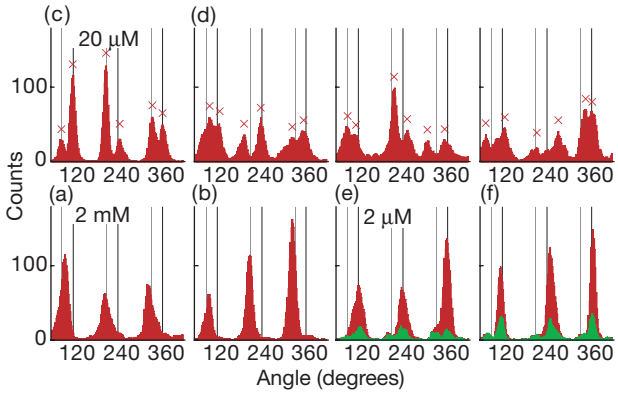

Figure 5 Histograms of angular positions over 0.5 s runs. Labels (a–f) are from records of which Fig. 4, **a**–**f** are a part. Each time course was passed through a five-point median filter, and its histogram was calculated with 2° bins. The histogram was then averaged over 10° intervals. Green parts (**e** and **f**) indicate 2 ms before and after main steps. Crosses indicate peaks identified by eye. To assess the baseline noise in raw data, we also constructed unfiltered, unaveraged histograms at 2 μM ATP with 2° bins (not shown). The histograms gave three peaks, of which the half width at 1/e height was estimated by fitting each peak with a gaussian curve; the half widths averaged 18° ± 7° (mean ± s.d. for 15 peaks).

imposed in Fig. 6a. The average (thick cyan line) shows that a whole 120° step completes within 0.25 ms (two frames) at saturating ATP. This value is an upper boundary because faster transients are unresolved with the camera that we used. Thus, time for the mechanical stepping (the times needed to reorientate the γ-subunit through 90° and 30°) occupies < 10% of the ATPase cycle time. The 90° substeps at 2 μM ATP are also within 0.25 ms (Fig. 6b). Stepping is fast, the instantaneous speed being well above 1,000 r.p.s., whether [ATP] is above or below K_m for rotation.

Substeps of 90° by ATP binding and 30° by product release

Figure 6c shows averages of all steps observed at indicated [ATP]. Presence of distinct and fast ~90° substeps is clear at all [ATP] < 60 μM, although whether the remaining ~30° is also stepwise cannot be judged in this figure. Fit with grey lines indicates the substep size to be 90.2° ± 0.3°.

The averaging was made after steps other than the central one were eliminated from each step record, such that it started with a near −30° dwell and ended with a ~120° dwell. When the last dwell at 120° was too short to be distinguished, the previous dwell at ~90° was extended to the right edge of the figure (see Methods). Thus, the portion of the curves between −30° and 0° reflects the distribution of dwell times at 0° that were started at the end of a substep from −30° to 0°, and terminated by a central 90° substep. The dwell is [ATP]-dependent, and can be explained by termination by ATP binding at the rate $k_{on}^{ATP} = 3.0 \times 10^7\ M^{-1}\ s^{-1}$ estimated from Fig. 8 (Fig. 6c; grey lines). The kinetics above 90°, in contrast, is [ATP]-independent, except that the amplitude decreases with [ATP]. The decrease is accounted for by the fact that, at [ATP] > K_m, the dwell at ~120° becomes too short and is not represented in our averaging procedure. As shown (grey lines), the kinetics are in accord with the scheme in Fig. 7a where two ~1-ms reactions govern the dwell at ~90° (the two reactions are deduced from Fig. 8).

Our proposed scheme is summarized in Fig. 7a. ATP binding drives a 90° substep (A→B). Next are hydrolysis reactions that are mechanically silent (B, C). Eventually, the last hydrolysis product of the previously bound ATP (ADP, phosphate, or both) is released, accompanying a 30° substep (C→A′) and resetting the system to the initial A state except for the 120° rotation that has taken place. At high [ATP], another 90° substep occurs immediately, and thus the two substeps are not resolved (Fig. 7b)—this is why we propose that both of the hydrolysis products must have been released by the end of a 30° substep. At [ATP] ~ K_m, ATP binding and hydrolysis take similar time, and 90° and 30° substeps are equally spaced.

Two ~1-ms reactions before a next step

Figure 8a shows histograms of dwell times between two main steps (90° or 120°) that were easily discerned at all [ATP]. At [ATP] ≪ K_m (0.02 and 0.2 μM), the histograms were fitted with a single exponential (pink lines) with a rate proportional to [ATP] (Fig. 8b; open cirlces), indicating that ATP binding alone sets the pace of rotation at these [ATP]. At 2 μM ATP, the histogram starts at the origin at zero dwell and shows a distinct peak, indicating the appearance of another rate-limiting reaction. Between 2 and 60 μM, the histograms are explained, roughly, by the ATP-binding reaction and an ATP-independent, ~0.5-ms^{-1} reaction (Fig. 8b). At [ATP] >> K_m = 15 μM, the histograms still show a distinct peak, indicating the presence of at least two reactions. A fit with two rate constants indicated both to be ~1 ms (Fig. 8b; filled black circles), which, taken together, can account for the 0.5-ms^{-1} reaction at intermediate [ATP]. Thus, at least three rate constants, two for the ~1-ms reactions and one for ATP binding, are required to describe the rotation kinetics at all [ATP]. Global fit to all histograms (green lines) showed k_{on}^{ATP} to be $(3.0 \pm 0.1) \times 10^7\ M^{-1}\ s^{-1}$ (consistent with the estimate from Fig. 3 (above) and previous values in actin[11] and single-fluorophore[18] assays), and the other two rates to be 1.64 ± 0.06 ms^{-1} and 0.71 ± 0.02 ms^{-1}. Of the latter two reactions, we cannot discriminate which is first, and the two rates do not differ significantly (see also Fig. 8b).

Thus we propose in Fig. 7a that two ~1-ms dwells separate the 90° and 30° substeps. A simple explanation is that the first dwell is terminated by release of a hydrolysis product (phosphate or ADP) and the second by release of the other product. Alternatively, the first reaction may be splitting of ATP to ADP and phosphate, and the second reaction the release of the two. Either interpretation is

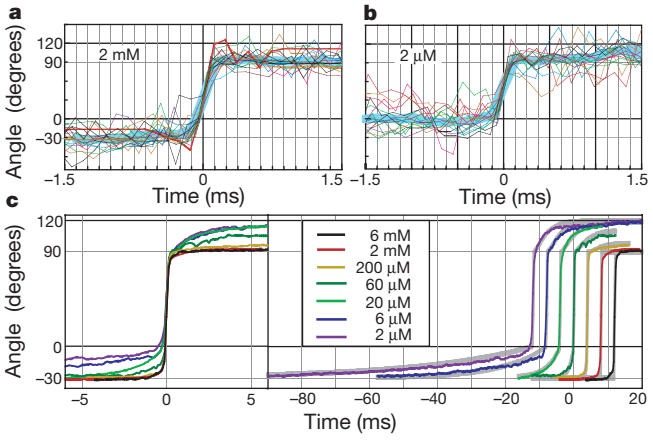

Figure 6 Kinetics of substeps. **a**, **b**, Eighteen consecutive steps and their average (thick cyan line) in a rotation record at 2 mM (**a**) or 2 μM (**b**) ATP (see Methods for the averaging procedure). **c**, Steps in several runs at indicated [ATP], averaged as in **a** and **b**. The averaging procedure retained all dwells at ~0° position in the ordinate, but some dwells at ~120° were converted to a horizontal line at ~90° position when the substep from 90° to 120° was contiguous (within 0.25 ms) with the next substep from 120° to 210°. This is why the curves at high [ATP] do not rise much beyond the 90° line. The curves are reproduced on the right; superimposed grey lines represent fits with theoretical curves based on the scheme in Fig. 7a (see Methods). The best fit was obtained with the size of the 30° substep, $A_{30°}$, of 29.8° ± 0.3° (mean ± s.e.m.).

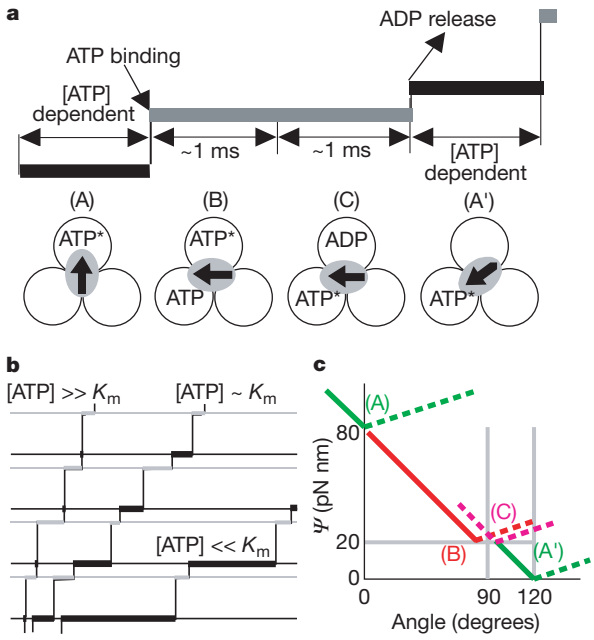

Figure 7 Proposed mechanism for F_1 rotation. **a**, Rotation scheme. ATP with asterisk represents ATP or ADP + phosphate; ADP (alone) may be phosphate or ADP + phosphate. **b**, Stepping time courses expected from **a**. **c**, Highly schematic diagram for the potential energy Ψ for γ-subunit rotation. Each coloured line shows Ψ in one of the four states in **a**. The orientation of the γ-subunit in state A (in **a**) is taken as 0°.

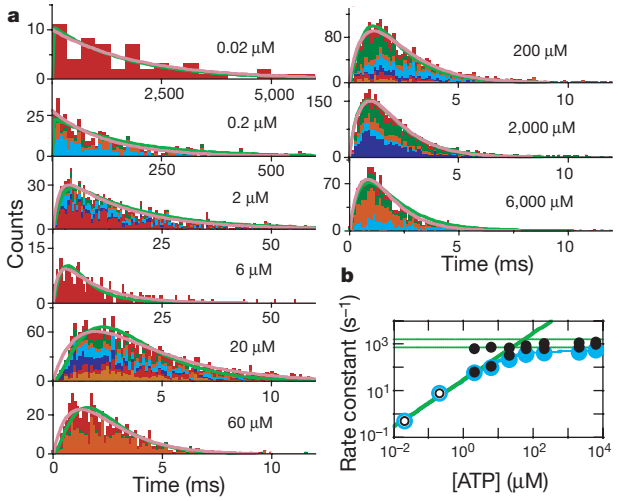

Figure 8 Dwells between main steps. **a**, Histograms of dwell times between two main (90° or 120°) steps at various [ATP]. Total counts in each histogram are 60, 463, 1,145, 2,862, 631, 2,384, 3,262 and 1,457 in the order of 0.02–6,000 μM. Histograms for individual runs are distinguished by colours; they are added to constitute a whole histogram. Pink lines at 0.02 and 0.2 μM ATP are single-exponential fits, constant·exp(–kt), with k shown in open circles in **b**. Pink lines at other [ATP] are fits with two rate constants, constant·[exp(–$k_a t$) – exp(–$k_b t$)], with k_a and k_b shown (filled black circles in **b**). Green lines show the result of a global fit to the individual histograms ($n = 38$; equal weight for each count) with sequential reactions (Fig. 7a) starting with ATP binding at the rate k_{on}^{ATP}[ATP] and two ATP-independent reactions with rates k_1 and k_2: $k_{on}^{ATP} = (3.0 \pm 0.1) \times 10^7\ M^{-1}\ s^{-1}$, $k_1 = 1.64 \pm 0.06\ ms^{-1}$, and $k_2 = 0.71 \pm 0.02\ ms^{-1}$ (s.e.m.). **b**, ATP dependence of the rate constants. Blue circles show the total rate, k or $k_a k_b/(k_a + k_b)$ for the individual fits. Green lines show the rate constants obtained in the global analysis, and the total rate, $[k_1^{-1} + k_2^{-1} + (k_{on}^{ATP}[ATP])^{-1}]^{-1}$, is shown by the blue line.

consistent with the biochemical evidence that the releases of ADP and phosphate occur at similar rates[21].

Discussion

In our rotation scheme (Fig. 7a) one or two of the three catalytic sites are filled at any time with ATP or its product(s) of hydrolysis. This is the so-called bi-site mechanism[2,3,17], which is the norm at least at submicromolar [ATP]. Previously we have demonstrated rotation at [ATP] as low as 20 nM, indicating that bi-site hydrolysis accompanies rotation[11] and that bi-site is the fundamental mode of rotation[17]. Present results suggest bi-site to be the norm also at physiological (mM) [ATP]. Alternation between two-filled and three-filled states (the tri-site mechanism) has been proposed for hydrolysis at high [ATP], from non-Michaelis–Menten kinetics[22,23] as in Fig. 3, and from quenching of tryptophan fluorescence in the active sites[24]. These results indicating the tri-site mechanism may have been influenced by the MgADP inhibition[25]. In contrast, ATP synthesis by ATP synthase is insensitive to the inhibition and seems to proceed by a bi-site mechanism[26]. Our rotation assay focuses only on active F_1, and is unaffected by the inhibition. The rotation rate was higher than one-third of the hydrolysis rate at all [ATP] (Fig. 3), implying that part of F_1 in solution was not fully active already at several seconds after exposure to ATP. We do not necessarily deny possible occupancy of three sites, but we claim that filling all sites does not significantly accelerate, nor add power to, rotation.

Presence of the substeps indicates the appearance of two metastable structures during rotation, in which the equilibrium positions of the γ-subunit differ by ~90° (Fig. 7a: A versus B or C). If our bi-site interpretation is correct, the crystal structure in Fig. 1a probably corresponds to the two-nucleotide structure B (or C). The other central structure with one nucleotide (A) is yet to be solved. A structure[27] reported recently indicates that the protruding portion of the γ-subunit, where the bead was attached, is torsionally flexible, therefore it is possible that the substeps revealed here might be an artefact: intrinsic steps of the γ-subunit are always 120°, whereas the bead is somehow obstructed at 90° and lags behind for a few ms. We dismiss this possibility because (1) the bead rotated over 120° within 0.25 ms at 2 mM ATP; (2) the dwell time at 90° was independent of the radius of bead rotation, which presumably reflects differences in bead attachment; and (3) larger beads did not show any sign of obstruction.

In Fig. 7a, binding of ATP drives the 90° substep. By reciprocity, the affinity of the β-subunit for ATP, on the left of the arrow on the central γ-subunit, must increase as the γ-subunit rotates[6,16,17,28]. Likewise, because release of ADP (or phosphate, or both) drives the 30° substep, the affinity of the β-subunit for ADP, on the right of the arrow, must decrease as the γ-subunit rotates over the last 30°. The magnitude of these affinity changes can be estimated as below. We have shown that, at least under a high load, F_1 does 80–90 pN nm of mechanical work per 120° step[11] and that the torque it produces is nearly independent of the rotation angle[16,17] (the potential energy Ψ for γ-subunit rotation is linearly downhill). Rotation of 291-nm beads gave similar results (R.Y., unpublished observations). These results, combined with Fig. 7a, suggest the diagram in Fig. 7c for Ψ: in state A in Fig. 7a, Ψ_A is minimal at 0°; ATP binding produces state B where Ψ_B is linearly downhill toward its minimum at ~90°; Ψ_C is also minimal at ~90°; product release recovers state A′ where $\Psi_{A'}$ is again linearly downhill toward 120°. Solid lines have the constant slope of 80 pN nm of work per 120° as indicated by experiment, whereas dashed lines are drawn arbitrarily to provide minima at experimental positions. Affinity for ATP is proportional to $\exp[(\Psi_A - \Psi_B)/k_BT]$, where k_BT ~4.1 pN nm is the thermal energy at room temperature[6,28]. Thus, rotation from 0° to 90° accompanies an increase in the affinity of more than $\exp[(60\ pN\ nm)/k_BT] \sim 2 \times 10^6$. The affinity for ADP, $\propto \exp[(\Psi_{A'} - \Psi_C)/k_BT]$, decreases more than $\exp[(20\ pN\ nm)/k_BT] \sim 10^2$.

These affinity changes account for ATP synthesis by forced clockwise rotation of the γ-subunit. Starting from state A′ in Fig. 7a, the affinity for ADP of the empty β-subunit on the right of the arrow increases as the γ-subunit rotates clockwise, and this β-subunit will pick up ADP from the medium. Further rotation decreases the affinity for ATP of the β-subunit carrying the previously synthesized ATP (on the left of the arrow), and this ATP will eventually be released. In this simple scheme, it is the central, asymmetrical γ-subunit that dictates which of the three β-subunits should change its affinity, and to what extent. A corollary of the 'γ-dictator model' is that tri-site operation may take place during hydrolysis if ADP release is somehow slowed down, for example by partial inhibition. After a 90° substep, the γ-subunit is already pointing close to the next β-subunit and signals this β-subunit to bind ATP. ATP binding may therefore occur without waiting for the 30° substep accompanying ADP release; however, this would be an inefficient tri-site mechanism with no additional power and speed, as we claim above.

Synthesis (or hydrolysis) of ATP on a β-subunit does not require much energy, because ATP and ADP + phosphate are in equilibrium on the β-subunit[21,26]. This is in accord with our observation that the hydrolysis reaction, which we presume to occur during the two ~1-ms reactions, is mechanically silent. The principal function of hydrolysis is to allow the release of bound ATP by converting it to products, thereby resetting the machine for the next round of stepping. Complete mechanical silence, however, is unfavourable for efficient ATP synthesis, because clockwise rotation should release ATP, not ADP + phosphate. Indeed, it has been indicated that the equilibrium shifts toward ATP during synthesis[26]. One such mechanism (a switch-less model for F_1 motor[16,17]) is suggested in Fig. 7c, where the minimum in Ψ_C (after hydrolysis) is placed slightly to the right of the minimum in Ψ_B (before hydrolysis). Such a slight shift would be undetectable at the present resolution.

Our work is essentially a consolidation and embodiment of the binding-change model[1–3]. Similar to F_1-ATPase, myosin hosts ATP and its hydrolysis product at near equilibrium[29,30]. This may be the general tactics adopted by many ATP-dependent molecular machines. If so, much of the free-energy drop accompanying ATP hydrolysis occurs in the ATP-binding step[17,29,30]. ATP binding may be the principal source of power in these molecular machines. Indeed, ATP binding induces large conformational changes in molecules such as myosin[31], kinesin[32,33] and chaperonin[34]. □

Methods

Proteins

A mutant (α-C193S, β-His_{10} at amino terminus, γ-S107C, γ-I210C) $\alpha_3\beta_3\gamma$ subcomplex (referred to here as F_1) derived from a thermophilic *Bacillus* PS3 was biotinylated at two cysteines (γ-107C and γ-210C) by incubation with fourfold molar excess of 6-*N*′-[2-(*N*-maleimido)ethyl]-*N*-piperazinylamidohexyl-D-biotinamide for 1 h at 23 °C. Unbound biotin was removed with PD10 (Amersham Pharmacia). Two biotin moieties per protein were found in an assay using 4-hydroxyazobenzene-2-carboxylic acid[35]. Eight molar excess of streptavidin (Pierce) was added to the biotinylated F_1 and purified on Superdex-200HR (Amersham Pharmacia).

Beads

Colloidal gold (diameter 40 nm; British BioCell International) was coated with biotinylated BSA by incubating 0.2% colloidal gold in 2 mM potassium phosphate pH 7.0 with 0.4 mg ml^{-1} BSA and 0.2 mg ml^{-1} sulphosuccinimidyl-*N*-[*N*′-(D-biotinyl)-6-aminohexanoyl]-6′-aminohexanoate (biotin-$(AC_5)_2$ sulpho-OSu; Dojin) for 1 h at 23 °C. We stored modified gold particles in a solution containing 2 mM potassium phosphate and 0.05% polyethylene glycol. Polystyrene beads were biotinylated as follows: 2.7% amino beads (108 nm; Polyscience) in 20 mM potassium phosphate pH 7.0 was incubated with 1 mg ml^{-1} of biotin-$(AC_5)_2$ sulpho-OSu for 1 h at 23 °C. We incubated 2.5% of carboxy beads (196 or 291 nm; Bangs) in 20 mM potassium phosphate with 3.6 mM 5-(((*N*-(biotinoyl)amino)hexanoyl)amino)pentylamine trifluoroacetate salt (Molecular Probes), 1% 1-ethyl-3-(3-dimethylaminopropyl)-carbodiimide hydrochloride and 1% *N*-hydroxysulphosuccinimide for 1 h at 23 °C.

Rate of ATP hydrolysis

Nucleotide-depleted F_1 was prepared[18], and its ATPase activity was determined at 23 °C with an ATP-regenerating system[18,36] containing 1 mM phosphoenolpyruvate, 200 μg ml^{-1} pyruvate kinase, 100 μg ml^{-1} lactate dehydrogenase, 0.15 mM NADH, and indicated MgATP in buffer A (50 mM KCl, 2 mM $MgCl_2$, 10 mM 3-[*N*-morpholino]propanesulfonic acid-KOH, pH 7.0). The initial hydrolysis rate was determined from the slope of absorbance decrease at 340 nm; the average slope was estimated for the period of 2–5 s (2 mM–12 μM ATP), 2–7 s (6–2 μM) or 2–12 s (0.2–0.06 μM) after the start of the reaction. In the presence of LDAO, hydrolysis kinetics showed a lag, and thus the rate was estimated at steady state during 400–500 s (2 mM–60 μM), 1,000–1,500 s (20–6 μM) or 4,500-5,000 s (2–0.6 μM).

Microscopy

Beads of 196 nm and 291 nm were observed with transmitted light on an Olympus IX-70 microscope. We observed 40-nm and 108-nm beads with laser dark-field microscopy[12] (Fig. 1c). A laser beam (532 nm, diameter 3 mm, 200 mW; Millenia II, Spectra Physics) was introduced into a dark-field condenser (numerical aperture, NA 1.2–1.4; Olympus) to illuminate the specimen obliquely. Light scattered by beads was collected with a ×100 objective (NA1.35; Olympus) with its iris diaphragm set to NA ~1.1 to block the direct ray. The field of view was ~50 μm. To confirm that we observed single 40-nm beads and not their aggregates, we measured the intensity of beads with regular dark-field microscopy with a halogen lamp, which provided homogeneous illumination. The intensity distribution had a single, large peak and a second small peak at four times the intensity of the first peak. Because an object smaller than the wavelength scatters light in proportion to the square of its volume[37], these peaks should correspond to single and duplex beads. Most beads were thus single. Twenty-fold reduction in the laser intensity did not affect the rotation speed, indicating that heating by the laser was insignificant.

Bead rotation assay

A flow cell was made of two KOH-cleaned coverslips separated by two spacers with 50 μm thickness[11]. Mixture of 0.1–1 nM beads and F_1 at 10–100 times the bead concentration in buffer B (buffer A plus 5 mg ml^{-1} BSA) was applied to the flow cell. Unbound beads were washed out with buffer B, and then buffer B plus MgATP (Mg^{2+} 2 mM in excess), 0.1 mg ml^{-1} creatine kinase, and 1 mM creatine phosphate was infused. Bead images were recorded as an eight-bit AVI file with a fast framing CCD camera (HiD-Cam, Nac) at 8,000 frames per s at [ATP] ≥ 2 μM; 125 frames per s at 0.2 μM; and 60 frames s^{-1} at 0.02 μM. The temperature was 23 °C. From each unmodified image, the bead centroid was calculated as $\Sigma x_i(I_i-I_{th})/\Sigma(I_i-I_{th})$, where x_i (or y_i) is the pixel coordinate, I_i the pixel intensity, I_{th} a threshold value, and the summation was for $I_I \geq I_{th}$.

The rotational frictional drag coefficient ξ for the beads was calculated as follows: for a single bead of radius a rotating in water with viscosity η (= 10^{-9} pN nm^{-2} s), minimal ξ is given by $8\pi\eta a^3$ when the rotation axis is at the bead centre, and maximal ξ by $8\pi\eta a^3 + 6\pi\eta a^3 = 14\pi\eta a^3$ when the axis is at a bead edge; for a bead duplex, minimal ξ is given by $2\times 8\pi\eta a^3 = 16\pi\eta a^3$ for a vertical duplex rotating around its centre, whereas maximal ξ is $2\times 8\pi\eta a^3 + 6\pi\eta a^3 + 6\pi\eta a\,(3a)^2 = 76\pi\eta a^3$ for a horizontal duplex rotating around an edge.

Analysis of substep kinetics

We superimposed and averaged time courses of individual steps as in Fig. 6a, b. First, we identified all main (90° or 120°) steps in a continuous run by eye. Then, individual steps were aligned on the time axis by positioning the midpoint of each step at time 0 (to within ± one frame). Vertical alignment was made by shift, by multiples of 120°. Next, steps other than the central one were eliminated from individual step records: the part earlier than 0.25 ms after the preceding 90° substep (or 120° step when substeps were contiguous) was replaced with a horizontal line at the angle at the 0.25-ms point (for example, a red line in Fig. 6a), and the part later than 0.25 ms before the following 90° substep (or 120° step) was replaced with the angle at that point (Fig. 6a; red line). Finally, we averaged all step records (Fig. 6a, b; thick cyan lines).

Step records averaged over several runs (Fig. 6c; coloured lines) were fitted with theoretical kinetics (Fig. 6c; grey lines) on the basis of the scheme in Fig. 7a; rate constants in the scheme were fixed to the values determined in Fig. 8. For the [ATP]-dependent kinetics for the rise from −30° to 0°, the grey lines show $A_{30°}\cdot\exp(k_{on}^{ATP}[ATP]t) - A_{30°}$, where $A_{30°}$ is the size of the 30° substep, $k_{on}^{ATP} = 3.0\times10^7$ M^{-1} s^{-1}, and t (< 0) is time from the central 90° substep. For the rise from 90° to 120°, two reactions with rates $k_1 = 1.64$ ms^{-1} and $k_2 = 0.71$ ms^{-1} are assumed, giving $A_{30°}\cdot B\cdot\{1-[k_2\exp(-k_1t) - k_1\exp(-k_2t)]/(k_2-k_1)\} + (120°-A_{30°})$ where $B = \exp(-k_{on}^{ATP}[ATP]\cdot 0.25\text{ ms})$ accounts for the loss of some of the 30° substeps in the averaging process . Global fit to all experimental curves (allowing a vertical shift for each curve) yielded $A_{30°} = 29.8 \pm 0.3°$.

Received 4 October 2000; accepted 26 February 2001.

1. Boyer, P. D. & Kohlbrenner, W. in *Energy Coupling in Photosynthesis* (eds Selman, B. R. & Selman-Reimer, S.) 231–240 (Elsevier, Amsterdam, 1981).
2. Boyer, P. D. The binding change mechanism for ATP synthase—some probabilities and possibilities. *Biochim. Biophys. Acta* **1140,** 215–250 (1993).
3. Boyer, P. D. Catalytic site forms and controls in ATP synthase catalysis. *Biochim. Biophys. Acta* **1458,** 252–262 (2000).
4. Cox, G. B., Jans, D. A., Fimmel, A. L, Gibson, F. & Hatch, L. The mechanism of ATP synthase. Conformational change by rotation of the b-subunit. *Biochim. Biophys. Acta* **768,** 201–208 (1984).
5. Mitchell, P. Molecular mechanics of protonmotive F_oF_1 ATPases. Rolling well and turnstile hypothesis. *FEBS Lett.* **182,** 1–7 (1985).
6. Oosawa, F. & Hayashi, S. The loose coupling mechanism in molecular machines of living cells. *Adv. Biophys.* **22,** 151–183 (1986).
7. Abrahams, J. P., Leslie, A. G. W., Lutter, R. & Walker, J. E. Structure at 2.8 Å resolution of F_1-ATPase from bovine heart mitochondria. *Nature* **370,** 621–628 (1994).
8. Duncan, T. M., Bulygin, V. V., Zhou, Y., Hutcheon, M. L. & Cross, R. Rotation of subunits during catalysis by *Escherichia coli* F_1-ATPase. *Proc. Natl Acad. Sci. USA* **92,** 10964–10968 (1995).
9. Sabbert, D., Engelbrecht, S. & Junge, W. Intersubunit rotation in active F-ATPase. *Nature* **381,** 623–625 (1996).
10. Noji, H., Yasuda, R., Yoshida, M. & Kinosita, K. Jr Direct observation of the rotation of F_1-ATPase. *Nature* **386,** 299–302 (1997).
11. Yasuda, R., Noji, H., Kinosita, K. Jr & Yoshida, M. F_1-ATPase is a highly efficient molecular motor that rotates with discrete 120° steps. *Cell* **93,** 1117–1124 (1998).
12. Kudo, S., Magariyama, Y. & Aizawa, S. Abrupt changes in flagellar rotation observed by laser dark-field microscopy. *Nature* **346,** 677–680 (1990).
13. Miyata, H. *et al.* Stepwise motion of an actin filament over a small number of heavy meromyosin molecules is revealed in an *in vitro* motility assay. *J. Biochem. (Tokyo)* **115,** 644–647 (1994).
14. Weber, P. C., Ohlendorf, D. H., Wendoloski, J. J. & Salemme, F. R. Structural origins of high-affinity biotin binding to streptavidin. *Science* **243,** 85–88 (1989).
15. He, X. M. & Carter, D. C. Atomic structure and chemistry of human serum albumin. *Nature* **358,** 209–215 (1992).
16. Kinosita, K. Jr, Yasuda, R. & Noji, H. F_1-ATPase: a highly efficient rotary ATP machine. *Essays Biochem.* **35,** 3–18 (2000).
17. Kinosita, K. Jr, Yasuda, R., Noji, H. & Adachi, K. A rotary molecular motor that can work at near 100% efficiency. *Phil. Trans. R. Soc. Lond. B* **355,** 473–489 (2000).
18. Adachi, K. *et al.* Stepping rotation of F_1-ATPase visualized through angle-resolved single-fluorophore imaging. *Proc. Natl Acad. Sci. USA* **97,** 7243–7247 (2000).
19. Jault, J.-M. *et al.* The $\alpha_3\beta_3\gamma$ complex of the F_1-ATPase from the thermophilic *Bacillus* PS3 containing the $\alpha D_{261}N$ substitution fails to dissociate inhibitory Mg ADP from a catalytic site when ATP binds to noncatalytic sites. *Biochemistry* **34,** 16412–16418 (1995).
20. Matsui, T. *et al.* Catalytic activity of the $\alpha_3\beta_3\gamma$ complex of F_1-ATPase without noncatalytic nucleotide binding site. *J. Biol. Chem.* **272,** 8215–8221 (1997).
21. Cunningham, D. & Cross, R. L. Catalytic site occupancy during ATP hydrolysis by MF_1-ATPase. Evidence for alternating high affinity sites during steady-state turnover. *J. Biol. Chem.* **263,** 18850–18565 (1988).
22. Gresser, M. J., Myers, J. A. & Boyer, P. D. Catalytic site cooperativity of beef heart mitochondrial F_1 adenosine triphosphatase. Correlations of initial velocity, bound intermediate, and oxygen exchange measurements with an alternating three-site model. *J. Biol. Chem.* **257,** 12030–12038 (1982).
23. Jault, J.-M. *et al.* The $\alpha_3\beta_3\gamma$ subcomplex of the F_1-ATPase from the thermophilic *Bacillus* PS3 with the βT165S substitution does not entrap inhibitory MgADP in a catalytic site during turnover. *J. Biol. Chem.* **271,** 28818–28824 (1996).
24. Weber, J., Wilke-Mounts, S., Lee, R. S., Grell, E. & Senior, A. E. Specific placement of tryptophan in the catalytic sites of *Escherichia coli* F_1-ATPase provides a direct probe of nucleotide binding: maximal ATP hydrolysis occurs with three sites occupied. *J. Biol. Chem.* **268,** 20126–20133 (1993).
25. Milgrom, Y. M., Murataliev, M. B. & Boyer, P. D. Bi-site activation occurs with the native and nucleotide-depleted mitochondrial F_1-ATPase. *Biochem. J.* **330,** 1037–1043 (1998).

26. Zhou, J.-M. & Boyer, P. D. Evidence that energization of the chloroplast ATP synthase favors ATP formation at the tight binding catalytic site and increases the affinity for ADP at another catalytic site. *J. Biol. Chem.* **268,** 1531–1538 (1993).
27. Gibbons, C., Montgomery, M. G., Leslie, A. G. W. & Walker, J. E. The structure of the central stalk in bovine F_1-ATPase at 2.4 Å resolution. *Nature Struct. Biol.* **7,** 1055–1061 (2000).
28. Wang, H. & Oster, G. Energy transduction in the F_1 motor of ATP synthase. *Nature* **396,** 279–282 (1998).
29. Wolcott, R. G. & Boyer, P. D. The reversal of the myosin and actomyosin ATPase reactions and the free energy of ATP binding to myosin. *Biochem. Biophys. Res. Commun.* **57,** 709–716 (1974).
30. Mannherz, H. G., Schenck, H. & Goody, R. S. Synthesis of ATP from ADP and inorganic phosphate at the myosin-subfragment 1 active site. *Eur. J. Biochem.* **48,** 287–295 (1974).
31. Houdusse, A., Szent-Györgyi, A. G. & Cohen, C. Three conformational states of scallop myosin S1. *Proc. Natl Acad. Sci. USA* **97,** 11238–11243 (2000).
32. Rice, S. *et al.* A structural change in the kinesin motor protein that drives motility. *Nature* **402,** 778–784 (1999).
33. Schnitzer, M. J., Visscher, K. & Block, S. M. Force production by single kinesin motors. *Nature Cell Biol.* **2,** 718–723 (2000).
34. Sigler, P. B. *et al.* Structure and function in GroEL-mediated protein folding. *Annu. Rev. Biochem.* **67,** 581–608 (1998).
35. Kunioka, Y. & Ando, T. Innocuous labeling of the subfragment-2 region of skeletal muscle heavy meromyosin with a fluorescent polyacrylamide nanobead and visualization of individual heavy meromyosin molecules. *J. Biochem. (Tokyo)* **119,** 1024–1032 (1996).
36. Kato, Y., Sasayama, T., Muneyuki, E. & Yoshida, M. Analysis of time-dependent change of *Escherichia coli* F_1-ATPase activity and its relationship with apparent negative cooperativity. *Biochim. Biophys. Acta* **1231,** 275–281 (1995).
37. Born, M. & Wolf, E. *Principles of Optics* 7th edn. (Cambridge Univ. Press, Cambridge, 1999).

Supplementary information is available on *Nature's* World-Wide Web site (http://www.nature.com).

Acknowledgements

We thank T. Ariga for sample preparation; A. Kusumi for colloidal gold; T. Hisabori, E. Muneyuki, T. Nishizaka, K. Adachi, C. Gosse, M. Y. Ali, S. Ishiwata and G. W. Feigenson for critical discussions; and H. Umezawa for laboratory management. This work was supported in part by Grants-in-Aid from the Ministry of Education, Science, Sports and Culture of Japan.

Correspondence and requests for materials should be addressed to K.K.